Research Square

Preprints are preliminary reports that have not undergone peer review.
They should not be considered conclusive, used to inform clinical practice,
or referenced by the media as validated information.

Nanostructure-engineered telecom quantum platform with room-temperature optical quantum coherence

Spyros Galis

sgalis@albany.edu

College of Nanotechnology, Science, and Engineering, University at Albany https://orcid.org/0000-0003-3872-1172

Alexander Kaloyeros

College of Nanotechnology, Science, and Engineering, University at Albany

Natasha Tabassum

College of Nanotechnology, Science, and Engineering, University at Albany

Article

Keywords:

Posted Date: November 27th, 2026

DOI: https://doi.org/10.21203/rs.3.rs-11789687/v1

License: This work is licensed under a Creative Commons Attribution 4.0 International License.
Read Full License

Additional Declarations: Yes there is potential Competing Interest. Please find pertinent information relating to one patent and two provisional patent applications for this technology: App. No.: 010-25-42WO01 Filing Date: 6/25/2025 Applicant: Research Foundation for SUNY First Named Inventor: Spyridon Galis Title: QUANTUM PHOTONIC COMPONENTS INCLUDING NANOSTRUCTURES AND METHODS OF FORMING NANOSTRUCTURES Status: Pending App. No.: 63/932,198 Filing Date: 12/5/2025 Applicant: Research Foundation for SUNY First Named Inventor: Spyridon Galis Title: Room Temperature Quantum Processor Based On On-Chip Arrays of Single-Ion Qudits Enabled by Materials Science and Engineering Status: Pending App. No.: 63/959,335 Filing Date: 1/13/2026 Applicant: Research Foundation for SUNY First Named Inventor: Spyridon Galis Title: Scalable and Telecom Single-Erbium System with Record-Long Room-Temperature Quantum Coherence Status: Pending

Nanostructure-engineered telecom quantum platform with room-temperature optical quantum coherence

Authors: Alex Kaloyeros, Natasha Tabassum, and Spyros Gallis*

Affiliations:

College of Nanotechnology, Science, and Engineering (CNSE), Department of Nanoscale Science and Engineering, University at Albany (UAlbany), NY 12222, USA

Abstract: Achieving μs-scale quantum coherence at room temperature in the telecom C-band remains a central challenge for solid-state quantum platforms, previously demonstrated only under vacuum cryogenic conditions. Here we introduce a CMOS-compatible nanoengineering approach that deterministically controls the number of erbium ions within a nanoscale volume and their electromagnetic environment using sub-5-nm silicon-based hollow nanopillars. This achieves the first geometry-defined spatial isolation of single erbium ions, suppressing ion-ion interactions and local electromagnetic-field noise under ambient conditions. Individually addressable single-ion devices exhibit a record room-temperature optical coherence time of T_2^*= 32 μs, limited by laser coherence, while photon-echo measurements yield coherence exceeding 60 μs at few-ion sites. We further demonstrate the first background-free, upconversion-enabled single-photon emission from multi-energy-level single erbium ions. The results establish nanostructure-engineered control of the local ion environments as a pathway toward scalable, manufacturable, telecom-compatible quantum networks, distributed sensing, and cryogenic-free quantum photonic integrated circuits.

A central challenge in solid-state telecom quantum systems is preserving long-lived quantum coherence without cryogenic cooling.[1-5] Although microsecond-scale coherence has been demonstrated at cryogenic temperatures, achieving comparable performance at room temperature has not yet been achieved. [3, 4, 6, 7] Addressing this limitation while maintaining CMOS-compatible fabrication and telecom C-band operation is essential for scalable quantum photonic integrated circuits (qPICs), [8-10] quantum networks, and distributed sensing. Eliminating cryogenic requirements would also substantially reduce the size, weight, power, and cost (SWaP+C) of deployable quantum technologies. [4] On-chip quantum systems, based on telecom quantum emitters and qubits (including, potentially, higher-dimensional (*d*) qudits, with $d > 2$ energy levels) that operate in the low-loss telecom band (e.g., the C-band around 1540 nm) and are compatible with fiber networks,[6, 11-13] can form the technological foundation of next-generation quantum information science (QIS) applications, such as long-distance quantum networking, quantum information storage and processing, and distributed quantum sensing and computing.[13-15]

Solid-state quantum systems, including semiconductor quantum dots, [16-18] defects,[19-21] and rare-earth-erbium (Er^{3+}) ions,[5-7, 22-27] have enabled pioneering advances in quantum functionality

such as state-of-the-art sensing[28, 29] in the near infrared range (1000 nm - 1300 nm), spin-photon interfaces[25, 30] and microsecond-scale coherence and coherent control in the telecom C-band. [7, 24, 26, 27] albeit under controlled laboratory vacuum conditions at cryogenic temperatures below 0.5 K. In leading demonstrations, single Er^{3+} ions are typically addressed through spectral rather than spatial isolation, exploiting distinct optical frequencies to distinguish a target ion from neighboring ions within the excitation volume, numbering up to hundreds of optically active Er^{3+} ions surrounding the probed ion.[7, 24, 26] Although this enables selective optical addressing, surrounding ions remain present and can contribute to decoherence through ion-ion interactions and local electromagnetic-field fluctuations, which are commonly suppressed through cryogenic operation and external magnetic fields. More broadly, rare-earth ion coherence is affected by magnetic dipole-dipole coupling, spectral diffusion, and electric- and strain-field fluctuations associated with defects and structural disorder.[31, 32, 33] Spatially isolating individual Er^{3+} ions within nanoscale structures offers an alternative strategy for reducing these interactions and suppressing local environmental noise (**Supplementary Figure S1Ai**). To our knowledge, such spatial isolation of single Er^{3+} ions has not previously been demonstrated. Existing quantum systems have yet to simultaneously achieve long-lived room-temperature optical coherence, native telecom C-band operation, and compatibility with scalable CMOS fabrication (**Supplementary Table S1**).

To this end, we introduce a CMOS-compatible nanoengineering approach that deterministically controls the number of Er^{3+} ions within a nanoscale volume and their electromagnetic environment. Our platform integrates Er^{3+} ions into silicon-based (silicon carbide (SiC) and silicon oxycarbide (SiC_xO_y)) hollow nanopillars (HNPs) with sub-5 nm critical dimensions, defined through conformal deposition rather than lithographic resolution. SiC and SiC_xO_y, as host matrices for Er^{3+}, offer unique fundamental and silicon-technology advantages.[34-36] For example, amorphous-SiC-on-insulator (a-SiCOI) [37] offers CMOS compatibility, a wide bandgap, a high refractive index ($n \approx 2.6$ at 1550 nm), and strong electro-optic properties.[37, 38] The self-aligned HNP geometry enables spatial isolation of individual Er^{3+} ions with nanometer-scale placement accuracy, minimizing neighboring ion interactions and associated dephasing. Combined with materials engineering that enhances the effective Er^{3+} excitation cross section by 2-3 orders of magnitude, this approach enables optical addressing and coherent control of single Er^{3+} ions under ambient conditions without using optical cavities. By systematically reducing the number of addressed ions from ensembles (60, 20, and 9 ions) to single ions, we demonstrate a greater than 1000-fold improvement in optical coherence, accompanied by enhanced Rabi oscillation visibility and reduced Raby decay times. This culminates in individually addressable single-ion devices exhibiting high-contrast Rabi oscillations (>96%) and room-temperature optical quantum coherence in the telecom C-band, providing a route toward scalable, cryogenic-free quantum photonic systems.

Our single-Er-ion quantum devices exhibit room-temperature performance ($T_2^* = 32$ μs) comparable to coherence times previously achieved under cryogenic conditions (≤0.5 K, see **Table S1**). [7, 24-27, 39] These results demonstrate that long-lived coherent control is possible under practical, ambient conditions. We further demonstrate high-purity single-photon emission through upconversion-mediated pathways involving the multi-energy-level structure of Er^{3+}, enabling optical readout at visible wavelengths (e.g., 520 nm) without optical cavities. Together, these results demonstrate a telecom- and CMOS-compatible engineering strategy, combining materials engineering and nanoengineering.

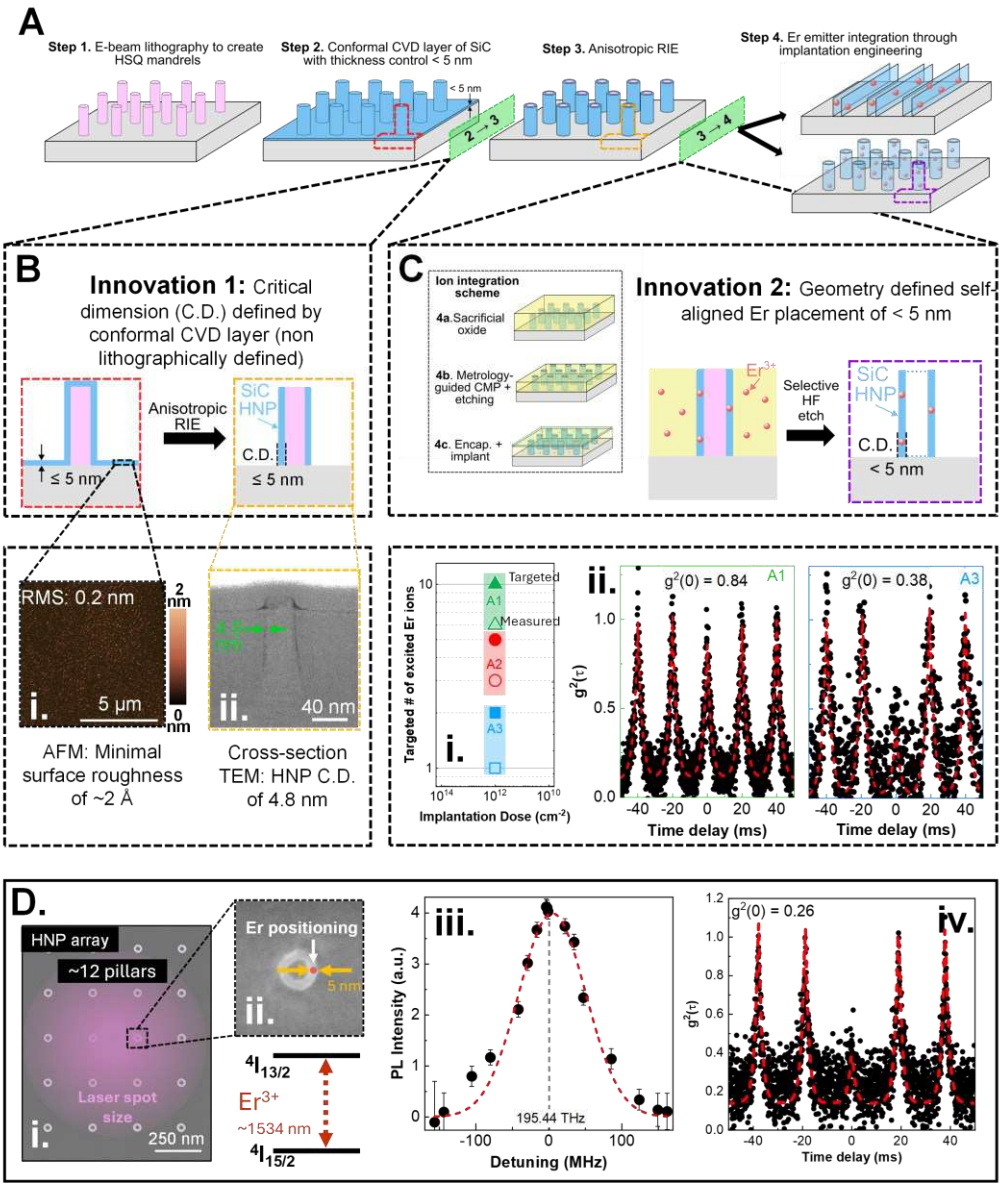


Figure 1: Key-enabling nanofabrication for integration of single-Er-ions in Si-based HNP arrays. A. Nanofabrication sequence and innovations for Er in engineered Si-based (SiC_xO_y) nanostructures, including HNP and NW arrays. **B.** *Innovation 1*: Highly conformal CVD enables C.D. control below lithographic resolution limits (≤5 nm), defined by deposition layer thickness rather than lithography. **i.** AFM image of Si-based films showing RMS roughness of ~2 Å. **ii.** Cross-sectional TEM of an HNP with a C.D. (sidewall) of ~4.8 nm. **C.** *Innovation 2*: Geometry-driven self-aligned ion placement, where the nanostructure sidewall serves as an implantation aperture, confining ions with <5 nm accuracy. **i.** For HNP arrays, four designs target 10, 6, 2, and 1 optically active Er^{3+}-ions within a 3×4 array. **ii.** Representative $g^2(\tau)$ measurements, with $g^2(0)$ values ranging from 0.84 (multi-ion, A1) to 0.38 (A3), with fits shown as red dashed lines to Equation 4 (Methods). **D. i.** Top-down SEM image of a representative 3×4 HNP array, and **ii.** a single HNP highlighting Er confinement within the ~5 nm sidewall. **iii.** Room-temperature PLE spectrum of a single-Er^{3+} in an A3 3×4 HNP array exhibiting the distinct telecom C-band optical Z_1 - Y_1 transition ~195.44 THz (~1533.9 nm) with a linewidth of ~67 MHz. Gaussian fit used to extract the FWHM is shown as red dashed line. **iv.** Corresponding g^2 correlation measurement showing a $g^2(0) = 0.26$, confirming single photon emission from a spatially resolved single Er^{3+} ion. Red dashed line shows fitting to Equation 4. Together, these structures establish geometry-defined control of the optically addressed Er^{3+} population from the ensemble to the spatially isolated single-ion regime.

This work could facilitate advanced telecom QIS technologies that could extend the range of practical applications in quantum sensing and imaging for biomedical applications, and in quantum sensing and reference systems (clock synchronization, distributed computation)[4] for a future Quantum Internet of Things.[13, 40]

Nanostructure-engineered isolation of single Er^{3+} ions

Figure 1 outlines the key-enabling nanofabrication innovations underlying the Er-doped Si-based HNP array platform, extending our previously reported Er-doped nanowire (NW) approach[41] to single-ion devices. Innovation 1 (**Figure 1B**) demonstrates non-lithographic route for defining critical dimensions (C.D.) ≤ 5 nm through highly conformal chemical vapor deposition (CVD)[33,41] with growth rates of 0.4 Å/s. Sacrificial mandrels defined by electron-beam lithography (pink in **Figure 1A**) serve as geometric scaffolds, while the thickness of the conformally deposited Si-based layer (a-SiC or a-SiC_xO_y),[41] determines the final nanostructure dimensions independently of lithographic resolution. Subsequent selective reactive-ion etching produces hollow stoichiometric HNPs with uniform, sub-5 nm sidewalls and minimal surface roughness (~2 Å RMS). By decoupling C.D. control from lithography resolution and avoiding the traditional etch steps, this approach minimizes sidewall roughness and associated fabrication-induced surface disorder. [42]

Deterministic integration of single ions with nanometer-scale spatial accuracy,[43] is central to scalable single-ion quantum devices.[31, 44, 45] We achieve geometry-defined ion placement with <5 nm accuracy by exploiting the HNPs as lateral implantation apertures (Innovation 2, **Figure 1C**). Following removal of the sacrificial oxide used during implantation, Er^{3+} ions remain confined within the Si-based nanostructures (hereafter referred to as Er:HNP or Er:NW). This geometry-defined confinement strategy is broadly applicable to any class of ion or defect introduced via implantation. Ion placement is controlled through a metrology-guided process that determines etch stopping point and aligns the implanted Er depth profile with the HNP height. To achieve single-ion isolation, we developed a geometry- and dose-based design framework correlating implantation dose, post-implantation processing, and nanostructure volume (**Supplementary Figures S2, S3**). **Supplementary data in Figure S3** summarize the representative nanostructure arrays investigated in this study, designated as HNP1, along with the calculated number of excited Er^{3+} ions for each configuration. Reducing the implantation dose or effective nanostructure volume progressively decreases the number of Er^{3+} ions within the optical excitation volume, enabling a transition from multi-ion ensembles toward the single-ion regime. To account for the stochastic nature of ion implantation, HNP1 arrays were designed such that multiple HNPs could be simultaneously illuminated within the telecom excitation beam, increasing the probability of detecting an isolated single ion. At λ = 1534 nm and an objective NA = 0.9, ~12 HNPs fall within the excitation spot's FWHM diameter (**Figure 1D i**). Each HNP1 array comprises a $10^3 \times 10^3$ lattice distributed over a 250 × 250 μm² area with a 250 nm pitch. Three representative arrays (A1, A2, A3), designed for progressively reduced Er^{3+} populations ($N_{\#}$) ranging from ~10 ions (A1) to ~2 ions (A3) per excitation volume, were investigated to characterize the transition from ensemble to single-ion quantum emission (**Supplementary Figure S3**). Room-temperature (RT) pulsed second-order photon-correlation measurements ($g^2(\tau)$), under resonant telecom excitation confirmed quantum emission from representative sites across the HNP1 arrays. Fitting the correlation functions (Equation 4 in **Methods**)[46] yields $g^2(0)$ values consistent with the targeted $N_{\#}$ (where $g^2(0) = (N_{\#} - 1)/N_{\#}$). Representative sites exhibited $g^2(0) = 0.84 \pm 0.02$ (~6 emitters, A1), and $g^2(0) = 0.38 \pm 0.03$ (~1-2 emitters, A3) (**Figure 1C ii**). At another A3 site, $g^2(0) = 0.26$

± 0.03, confirmed single-photon emission from a spatially isolated Er^{3+} ion (**Figure 1D iv**). To our knowledge, this represents the first spatial isolation of a single Er^{3+} ion without relying on spectral isolation. [5, 7, 22, 23, 47] RT photoluminescence-excitation (PLE) spectroscopy further revealed a telecom C-band transition centered at ~1533.9 nm with a measured linewidth of ~67 MHz (**Figure 1D iii**), limited by excitation laser broadening (see Methods).[48] To determine optimal implantation parameters, SRIM simulations guided the implantation parameters to control Er^{3+} placement while minimizing implantation-induced lattice damage (**see Methods)**. [49] This control is complemented by a materials-engineering strategy[50-52] aimed at improving the optical addressability of a few and single Er^{3+} ions at room temperature. Specifically, the Er^{3+} excitation cross-section, σ, is 2-3 orders of magnitude larger than typical values of ensemble rare-earth ions in bulk hosts.[33] **Figure S1** in the Supplementary illustrates the impact of this enhanced excitation cross-section by comparing resonant telecom power-dependent PL (PDPL) measurements from a representative Er:HNP array containing ~5 Er^{3+} ions with those from a pristine LN reference sample containing a comparable number of ions.

Ion-number-dependent optical coherence at room temperature

We use our nanoengineering approach to vary the number of Er^{3+} ions within the probe volume, and then directly track the resulting effects on optical coherence and Rabi dynamics (**Figure 2**). Ion populations were estimated using photon-correlation and power-dependent PL (PDPL) measurements, supplemented by upconversion PL count rates (**see Methods**). Sites containing approximately 60 ± 17, 20 ± 6, 9 ± 1, and 1 Er^{3+} ions exhibited upconversion count rates of ~38,100, ~19,450, ~10,250, and ~750 counts s^{-1}, respectively, matching within the uncertainty of the # of ions (**Supplementary Figure S4**). Rabi oscillations were measured using resonant pulsed excitation by varying the pulse width t_p at a fixed photon flux (φ= 5×10^{19} $cm^{-2}\cdot s^{-1}$). The integrated PL intensity was recorded as a function of t_p and was fit[24] using

$$I(t_p) = A[1 - \exp\left(-\frac{t_p}{T_{2,Rabi}}\right)\cos(2\pi f_{Rabi} t_p)] \ , \quad [1]$$

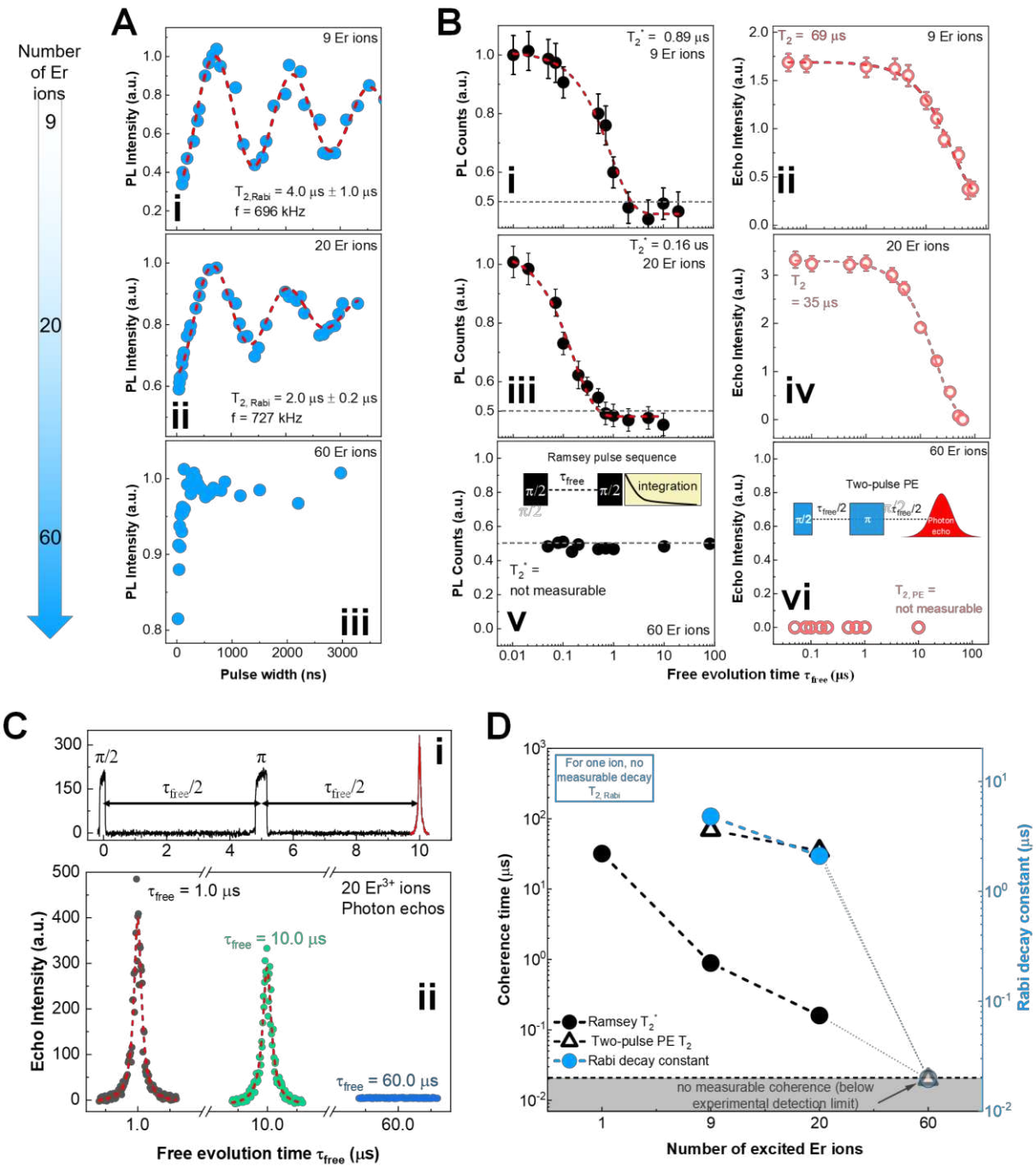


Figure 2: Effect of number of ions on Rabi oscillations and optical coherence. **A**. Rabi oscillation measurements (PL counts versus pulse width) for spots containing **i.** 9, **ii.** 20, and **iii.** 60 Er^{3+} ions (top to bottom). Oscillation visibility degrades with increasing ion numbers. Error is represented by the size of the points. **B.** Ramsey (T_2^*, black) and two-pulse photon-echo (T_2, red) measurements for 9 (**i, ii**), 20 (**iii, iv**), 60 (**v, vi**) Er^{3+} ions. Dashed lines are fits to Equations 2 and 3, yielding T_2^* = 0.89 µs and T_2 = 69 µs at 9 ions, T_2^* = 0.16 µs and T_2 = 35 µs at 20 ions, and no measurable coherence at RT for the 60 ions. Inset of v and vi: Ramsey and photon-echo pulsing sequences, respectively. **C. i.** Visualized two-pulse photon echo pulsing sequence in the time domain and **ii.** photon echoes from 20 Er ions for a τ_{free} of 1.0 µs, 10, and 60 µs. **D.** Comparison of coherence times and Rabi decay constants versus Er^{3+} ion number, including for a single Er ion for which no Rabi decay was observed over the measured pulse-width range (see Figure 3). The reduction in coherence with increasing ion number suggests ion-ion interactions as a significant room-temperature dephasing channel.

where t_p is the pulse width, f_{rabi} is the Rabi frequency, $T_{2,\,Rabi}$ is the Rabi decay time, and A is a fitting parameter. No resolvable Rabi oscillations were observed for ~60 ions, indicating a $T_{2,\,Rabi}$ below the detection limit (~20 ns). For ~20 ions, oscillations exhibited a $T_{2,\,Rabi}$ = 2.1 ± 0.2 μs, ~25% contrast, and f_{rabi} = 727 kHz. For ~9 ions, $T_{2,\,Rabi}$ increases to 4.0 ± 1.0 μs and the contrast to ~48%, with f_{rabi} = 696 kHz. At the single-ion limit, no measurable Rabi decay was observed over the investigated pulse-width range, with a contrast of >96% and f_{rabi} = 694 kHz (**Figure 3**). To investigate the corresponding ion-number dependence of optical coherence, we performed Ramsey and two-pulse photon echo measurements using π/2 (~360 ns) and π (~720 ns) pulses determined from the Rabi oscillations (see **Methods**). Ramsey measurements probe the decay of optical coherence between two π/2 pulses. The PL counts integrated after the second pulse were measured as a function of free evolution time and were fit to

$$I = I_0 e^{-\frac{\tau_{free}}{T_2^*}}, \qquad [2]$$

where τ_{free} is the free evolution time and T_2^* is the Ramsey optical coherence time. Under resonant excitation at 195.44 THz without detuning, no Ramsey oscillations are observed. Fits to Equation 2 yield T_2^* = 0.89 ± 0.11 μs for 9 ions, 0.16 ± 0.03 μs for 20 ions, and no measurable coherence at 60 ions (**Figure 2Bi, iii, v**). These coherence times are substantially shorter than the corresponding excited-state lifetimes (T_1 = 1.5 - 2.5 ms). We also performed two-pulse photon echo measurements, in which a π pulse following the initial π/2 pulse rephases the optical dipoles, producing a temporally localized echo less sensitive to laser phase fluctuations.[22] This echo provides an experimental signature of the preserved optical quantum coherence in the Er^{3+} system.[53] The time-resolved echo signal was integrated over the echo window at each τ_{free}. The integrated echo intensity was measured as a function of τ_{free} and were fit[26, 27] to

$$I = I_0 e^{-2\left(\frac{\tau_{free}}{T_2}\right)^x}, \qquad [3]$$

where τ_{free} is the free evolution time, and x = 1 due to the observed single-exponential decay of the echo intensity.[54] Fits to Equation 3 (**Figure 2Bii, iv, vi**) yield T_2 = 69 ± 2 μs for 9 ions, T_2 = 35 ± 2 μs for 20 ions, with no measurable coherence at 60 ions. Representative time-resolved echo signals from the site containing 20 Er^{3+} ions are shown in **Figure 2C**, with extended data shown in **Supplementary Figures S5 and S6**. The improvements observed in the optical coherence and Rabi oscillation visibility, shown comparatively together in **Figure 2D**, suggest that reducing the number of interacting Er^{3+} ions toward a single isolated ion suppresses dephasing at room-temperature. Confinement of the Er^{3+} ions within the 5 nm HNP geometry may thus provide an electromagnetic environment with reduced ion-ion interactions, defect-, strain-, and/or charge-induced dephasing, enabling longer optical coherence at room temperature.

Room-temperature coherent control of single Er^{3+} ions

To directly probe single-ion quantum behavior, several HNP array devices, which were engineered to target single isolated Er ions ($N_{\#}$ = 1), were fabricated, and spatially isolated Er ions were identified via upconversion-mediated confocal PL mapping. One representative image of an isolated Er^{3+} ion is shown in **Figure 3A,** with several others shown in **Supplementary data Figure S7**. Pulsed-g^2 measurements under telecom-resonant excitation at this site, labeled Q1, show pronounced antibunching with $g^2(0) = 0.09 \pm 0.02$, confirming single-photon emission from a spatially-isolated single-Er^{3+} ion (**Figure 3B**). Telecom time-resolved PL (TRPL) measurements acquired using time-correlated single photon counting (TCSPC) reveal a biexponential decay with components τ_1 = 0.3 ms and τ_2 = 1.3 ms, yielding an average excited-state lifetime T_1 of 1.2 ± 0.1 ms. An independent measurement of T_1, performed using a $\pi/2$ excitation pulse and monitoring the integrated photon counts as a function of delay after excitation, yielded a lifetime of 1.3 ms (**Supplementary Figure S8E**). PDPL measurements using resonant telecom excitation yield an effective excitation cross-section of $\sigma = \sim 5 \times 10^{-17}$ cm^2, with an onset saturation photon flux $\varphi_{sat} \simeq 10^{21}$ cm^{-2} s^{-1} (**Supplementary data Figure S8**), consistent with the measured value from the ensemble Er:HNP structures ($N_{\#}$= 5 ions, **Supplementary data Figure S1**). Under resonant pulsed excitation, coherent Rabi oscillations are observed from single Er^{3+} ions and fit with Equation 1 (**Figure 3C**). From the fit, a Rabi frequency, f_{Rabi}, of 694 kHz was extracted with a contrast of > 96%. To probe the optical coherence of the single ion, Ramsey measurements were performed at room temperature under excitation resonant with the $^4I_{13/2} \leftrightarrow {}^4I_{15/2}$ transition with no detuning (**Figure 3D**). The Ramsey sequence consists of two optical $\pi/2$ pulses, each with a width of 360 ns, separated by a variable free-evolution interval τ_{free}. Fitting the integrated PL counts to Equation 2 yields an optical coherence time $T_2^* = 32\ \mu s \pm 4\ \mu s$, nearly identical to the estimated coherence time of the PPCL550 excitation laser (~32 μs) as determined from frequency-noise power spectral density (PSD) measurements (see Methods). We also deduce the optical coherence time by fitting Ramsey oscillations measured under detuned excitation (Δf = 0.1 MHz), yielding a similar optical coherence time of $T_2^* = 29\ \mu s \pm 4\ \mu s$ (**Supplementary Figure S9**). This deduced optical coherence time is therefore likely a lower bound on the intrinsic optical coherence time of the single-Er:HNP platform ($T_2^* \geq 29\ \mu s$), owing to the finite coherence time of the excitation laser. Regardless, this value represents at least a three-order-of-magnitude increase in the optical coherence time T_2^*, from the value for 60 ions (<20 ns, the detection limit) to 32 μs for a single ion. This coherence time under ambient conditions demonstrates suppression of dephasing pathways in our Er:HNP (e.g., ion-ion and ion-defect interactions) and shows that quantum coherence can be preserved even without cryogenic cooling. In general, optical coherence time is ultimately limited by the excited state lifetime T_1 of the two-level Er system according to the relation $T_2^* \leq 2T_1$. **Figure 3E** visualizes this difference by comparing the excited-state population decay T_1 measured following a $\pi/2$ excitation pulse, with the T_2^* obtained from the Ramsey measurement, where the ratio between the two times $T_2^*/2T_1 = \sim 0.01$. As mentioned above, the intrinsic optical linewidth of the single Er^{3+} in SiC HNP is limited by the broadening of the tunable-telecom-laser. However, based on the observed optical coherence time of $T_2^* = 32\ \mu s$,

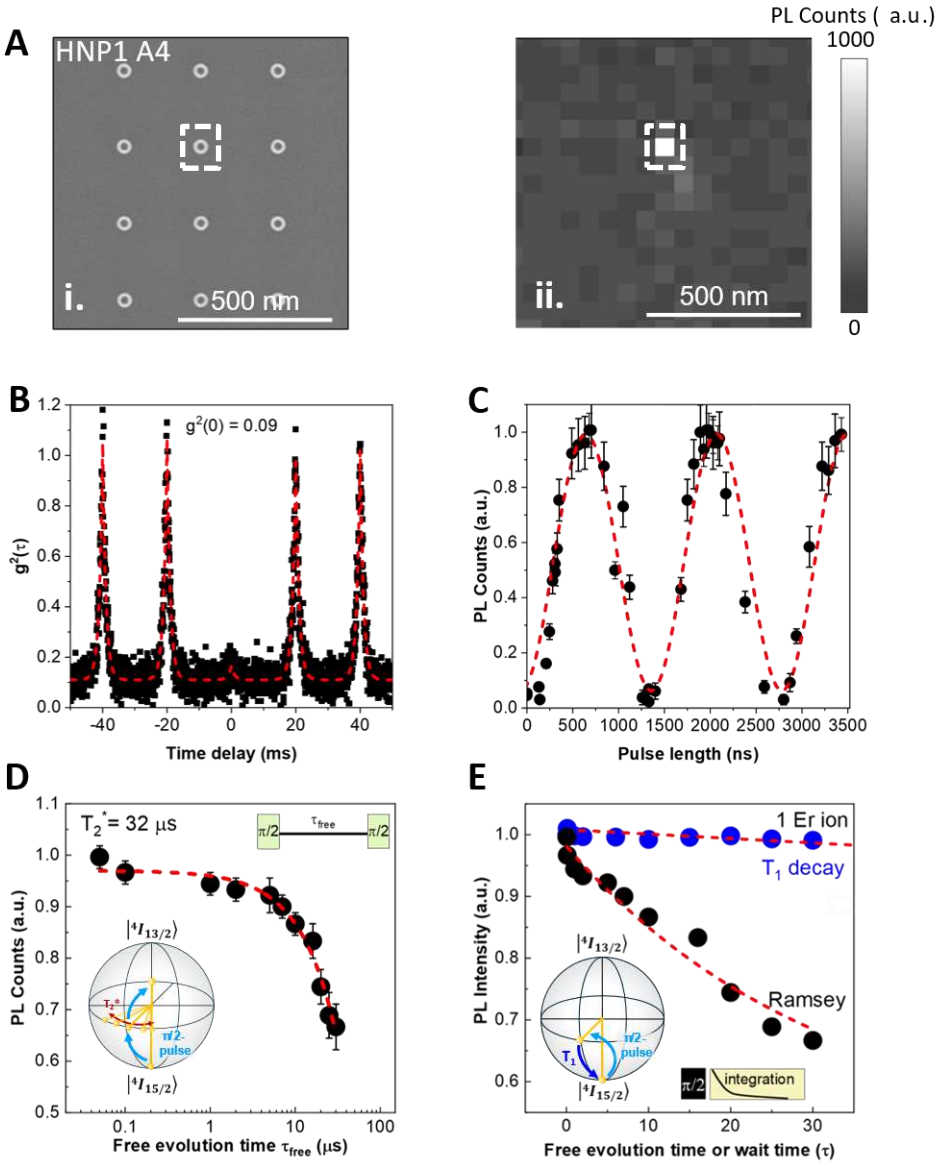


Figure 3: Room temperature properties of single-Er SiC HNP devices in the telecom-C band. **A. i.** SEM image of area representing a single Er qubit Q1 on the HNP1 (A4) and **ii.** corresponding upconversion PL image of the same area demonstrating spatial-isolation shown as PL counts from a single pixel. White box outlines same area in both images. **B.** $g^2(\tau)$ measurements of Q1 show pronounced antibunching under ~1534 nm excitation with $g^2(0) = 0.09$ determined from fit to Equation 4 (red dashed line), demonstrating single-photon emission. **C.** Rabi measurements on Q1 demonstrate coherent Rabi oscillations of the optical transition (f_{Rabi}= 694 kHz with contrast >96%). Fit to Equation 1 shown in red. **D.** Ramsey measurements on Q1 of the telecom Er transition. The extracted decay time T_2^* from fit to Equation 2 is 32 µs (red dashed line). The inset shows the Bloch sphere representation of the decoherence process of the single-Er^{3+} ion excited by a π/2 pulse. **E.** Comparison of the intensity decay measured from the Ramsey measurement with the measured excited-state lifetime T_1 = 1.2 ms, illustrating the coherence limit $T_2^* \leq 2T_1$, having $T_2^*/2T_1$ = ~0.01. Fits to exponentials are shown in red.

the corresponding optical linewidth is projected to be on the order of a few kHz $\left(\Delta\nu_0 = \frac{1}{\pi T_2^*} = \sim 10\ \text{kHz}\right)$.

Upconversion-enabled single-ion optical readout

To highlight the platform's broader quantum functionality and technological promise, we demonstrate upconversion imaging of the Er^{3+} emission, offering a pathway toward faster readout and sensing applications. We have implemented an upconversion-mediated pulse-sequence protocol to establish a background-free, high-efficiency optical readout pathway of the single-ion devices (Er:HNPs) and to access the multi-energy-level structure of the qubit devices (**Figure 4 and Supplementary Figure S4**). In this scheme, resonant telecom excitation at ~1533.9 nm using a sequence of N π pulses (N = 2-3) populates higher-lying excited states, giving rise to visible and near-infrared upconversion emission at ~520 nm, ~660 nm, and ~980 nm (see Methods for details). The corresponding energy-level diagram in **Figure 4A** illustrates potential excitation pathways, for example, of the $^2H_{11/2}$ manifold resulting in 520 nm upconverted emission excited using 3 sequential pulses. **Figure 4B** shows representative results from an isolated single-ion qubit (Q1). Upconverted PL at each wavelength is selectively collected using a corresponding bandpass filter and detected with a low-light single-photon camera (Andor DV437). We have achieved spatially-resolved imaging with sub-diffraction resolution (<70 nm, limited by the camera pixel resolution) enabled by the individual single-ion qubits (**Figure 4B i**). TRPL measurements of the upconverted emission yield lifetimes (T_1) of 164 μs, 380 μs, and 712 μs for the 520 nm, 660 nm, and 980 nm channels, respectively (**Figure 4B ii**). These lifetimes are substantially shorter than the 1.2 ms lifetime of the $^4I_{13/2}$ state, consistent with radiative decay from higher-lying excited states involved in the upconversion process. PLE spectroscopy of the upconverted emission (shown here for the 520 nm emission) yields an optical linewidth of ~27 MHz (**Figure 4C**). Pulsed-g^2 measurements of the upconverted emissions reveal high-purity single-photon Er-emissions. Representative examples are presented in **Figure 4D i, ii** for the 520 nm and 980 nm upconversion states, exhibiting enhanced $g^2(0)$ values of 0.06 ± 0.01 and 0.18 ± 0.03, respectively. The peak decay times (τ_{PL}) extracted from fitting the g^2 correlation spectra match the measured lifetimes (T_1) of the corresponding transitions, as summarized in **Supplementary Table S2** (see also Methods).

These results establish a CMOS-compatible, nanoengineered platform for spatially isolated single-Er^{3+} ions exhibiting coherent optical control at room temperature in the telecom C-band. Sub-5-nm nanostructuring suppresses dephasing, enabling laser-limited optical coherence of 32 μs, while upconversion-mediated pathways provide background-free, high-purity single-photon emission across multiple optical transitions. Together, these capabilities establish a manufacturable route toward cryogenic-free quantum photonic integrated circuits, scalable quantum networks, and distributed quantum sensing.

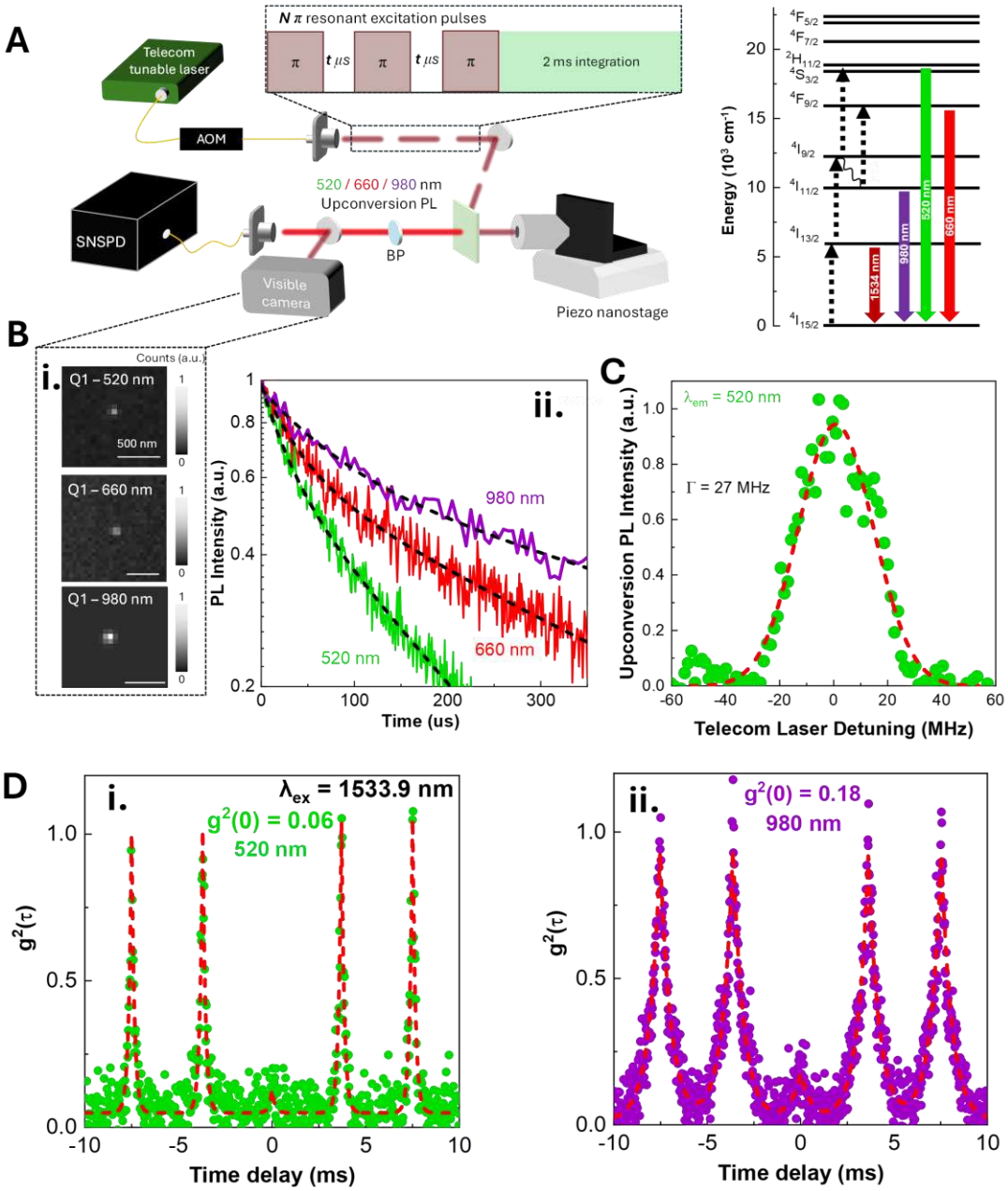


Figure 4: Upconversion-mediated control of the visible and NIR states of single-Er^{3+} qubits (multi-energy-level system). A. Schematic of the measurement setup and pulsing sequence used for upconversion-mediated PL and microscopy from single-Er^{3+} qubits. Two or three π telecom pulses resonant with the first excited energy level ($^4I_{13/2}$) with varied spacings are used to excite upconverted emission. Energy-level diagram for trivalent Er^{3+} showing the telecom (~1534 nm) as well as its distinct visible (~520, $^4I_{15/2} \leftrightarrow {}^2H_{11/2}$, and ~660 nm, $^4I_{15/2} \leftrightarrow {}^4F_{9/2}$) and NIR (~980 nm, $^4I_{15/2} \leftrightarrow {}^4I_{11/2}$) optical transitions involved in Er^{3+} luminescence. **B**. Upconversion PL characterization of a single-Er^{3+} qubit (Q1). **i.** Upconversion-based imaging showing a single-pixel (sub-diffraction) single-photon-emission spot corresponding to a single Er^{3+}-ion at three different wavelengths (520 nm, 660 nm, 980 nm). **ii.** Upconversion TRPL spectra showing emission at 520 nm, 660 nm, and 980 nm with lifetimes of 164 μs, 380 μs, and 712 μs, respectively. Dashed lines show exponential fits to extract lifetimes. **C.** Representative PLE with extracted optical linewidth of Q1 obtained via upconversion detection at 520 nm exhibits an optical linewidth of ~27 MHz at room temperature. The red dashed line shows a Gaussian fit. **D. i.** Single-photon emissions demonstrated for the single-Er^{3+} qubit at: **i.** 520 nm with $g^2(0) = 0.06$ (excitation with 3 sequential telecom pulses), and **ii.** 980 nm with $g^2(0) = 0.18$ (2 sequential telecom pulses). Red lines show fitting to Equation 4.

Acknowledgments: The authors gratefully acknowledge Souryaya Dutta and Kazy Shariar for their assistance with materials growth, CMP, and etching during nanofabrication. We also extend thanks to Pure Photonics for their technical support. This work was also supported by the College of Nanotechnology, Science, and Engineering (CNSE) Innovation Lab.

Funding: S.G. and A.K. were supported by the National Science Foundation under Grant No. 2138174-QuIC-TAQS. N.T. was supported by the National Science Foundation under Grant No. 1842350.

Author contributions: S.G. conceived and designed the experiments and methodology, including device nanofabrication, materials engineering, and quantum optics. A.K. and S.G. developed the experimental setup. A.K. fabricated the devices, performed the measurements, and analyzed the data. N.T. assisted with the growth, preparation, and measurements of 1st-generation nanostructures. S.G. assisted in device fabrication and quantum optics measurements. S.G. contributed to data analysis and advised on all efforts. A.K. and S.G. prepared the manuscript.

Competing interests: A portfolio of patent applications relating to this technology and innovations has been filed with the United States Patent & Trademark Office and is assigned to the Research Foundation for SUNY.

Data, code, and materials availability: The original contributions presented in this study are included in the article and supplementary material. Further inquiries can be directed to the corresponding author.

Methods

Nanofabrication and metrology

Supplementary data Figure S10 illustrates the nanofabrication process used to realize the ordered arrays of Er-doped silicon-based (e.g., silicon carbide (SiC) and SiC_xO_y) nanostructures (hollow nanopillars (HNPs) and nanowires (NWs)), referred to as Er:HNP or Er:NW. The process is compatible with CMOS manufacturing and enables independent control over the nanostructure geometry (diameter and critical dimension (C.D.) thickness), array periodicity, and controlled ion placement, potentially for any ion or defect compatible with ion implantation. While we use electron beam lithography (EBL) for rapid prototyping and device iteration, the device layouts and mandrel process are compatible with 300-mm wafer-scale lithographic manufacturing. For the structures presented in this work, the fabrication sequence begins with spin-coating a ~130 nm thick hydrogen silsesquioxane (HSQ) negative tone resist film onto a variety of substrates, including crystalline Si (e.g., Si (100) and Si (111)), thermally grown SiO_2-on-Si, and amorphous SiC on an insulator (a-SiCOI). Following a soft bake at 80°C for 4 minutes, EBL is used to define high-aspect ratio (~4:1 height:width) cylindrical or wire-like HSQ mandrels, which serve as sacrificial templates for subsequent nanostructure formation. Patterned samples are developed in a tetramethylammonium hydroxide (TMAH) solution bath, yielding a periodic HSQ ribbon array (pink in **Figure S10**). An a-SiC or oxygen co-doped a-SiC layer (a-SiC_xO_y, silicon oxycarbide) is subsequently deposited conformally by chemical vapor deposition (CVD) at 800°C (Step 2). The resulting film thickness is precisely controlled via growth time (e.g., ~4.8 ± 0.2 nm for the HNP arrays) as determined by ellipsometry, scanning electron microscopy (SEM), and transmission electron microscopy (TEM). The film stoichiometry can be continuously tuned from stoichiometric a-SiC to stoichiometric a-$SiC_xO_{2(1-x)}$ ($SiC_{0.5}O_{1.0}$) by adjusting the oxygen gas flow rate during growth, as detailed in previous reports.[50] This conformal deposition defines the

sidewalls around the HSQ mandrels, which ultimately set the C.D. of the resulting HNPs. A fluorine-based anisotropic reactive ion etching process (RIE) is used to remove excess deposited material from the substrate surface and the tops of the mandrels while preserving the conformal sidewalls. This step converts the deposited film into vertically aligned HNP structures that adopt the underlying cylindrical or wire mandrel geometry. The nanostructure width (or C.D.) is therefore dictated by the deposition thickness, while the diameter and array periodicity are dictated by the HSQ mandrels. **Supplementary data** in **Figure S10B, C** present angled and cross-section SEMs of the Si-based HNPs, respectively. To determine optimal implantation parameters, we employed SRIM simulations to model the depth distribution of implanted Er ions and accompanying profile of implantation-induced lattice damage. This SRIM-based framework for minimizing implantation-induced defects has been experimentally validated in our previous report on Er-implanted thin-film lithium niobate (Er:LN).[49] These simulations provide a quantitative relationship between Er implantation depth and the local density of implantation-induced vacancies within the volume surrounding each Er ion. By comparing the simulated vacancy density across implantation energies and oxide encapsulation thicknesses, we select conditions that place Er at the desired depth while reducing implantation-induced damage.

To enable deterministic integration of Er^{3+} ions, the fabrication process is extended beyond Step 3 following the RIE. An approximately 800 nm-thick sacrificial oxide layer is deposited by CVD to fully encapsulate the nanostructures and the remaining HSQ mandrels. The oxide surface is planarized using a multi-step chemical-mechanical polishing (CMP) process. A coordinated sequence of RIE steps and diluted hydrofluoric (DHF) etching, guided by a metrology protocol, is then used to recess the oxide to the precise height of the nanostructures. A second conformal oxide encapsulation layer is subsequently deposited on the planarized sample surface to control the ion-implantation range and, consequently, the number of ions incorporated into the nanostructures. In this study, Er ions are implanted at room temperature with an acceleration voltage of 100 kV and fluences ranging from 10^{12} to 10^{14} cm^{-2}. Post-implantation thermal annealing is performed at 900°C for 1 hour under argon and/or oxygen ambient to activate the Er^{3+} ions and repair implantation-induced lattice damage. Following annealing, both the sacrificial oxide and the encapsulation oxide layers can be removed using a DHF etch, along with the remaining HSQ. This etch process exhibits high selectivity between the oxide layers and the nanostructures, with an etch-rate contrast exceeding 10^3, leaving the Er:HNP or NW structurally intact, showing no measurable SiC or SiC_xO_y etching under the conditions used in this work. **Supplementary data Figure S11** presents representative PL results for an ensemble Er:NW array.

Calculations of system efficiency

To estimate the collection efficiency of the 100× objective (NA = 0.9), we treat the emitter as an isotropic point source. For an objective in air ($n \approx 1$), the numerical aperture defines the maximum collection angle via $NA = n \sin(\theta)$, giving $\theta = \arcsin(0.9) = 64°$. The corresponding solid angle is $\Omega = 2\pi (1 - \cos\theta)$, so the fraction of photons collected relative to the full 4π emission is: $\eta = (1 - \cos\theta) / 2 = (1 - 0.44) / 2 = 0.28$. Finite-difference time-domain simulations of the vertical extraction efficiency η_{ext} in the HNPs show that ~0.40 of the emitted power is extracted into the upper half-space. Within that upper half-space, the objective subtends a fraction $1 - \cos\theta = 0.56$, giving a net photonic collection efficiency: $\eta_{coll} = 0.40 \times 0.56 = 0.22$. This is multiplied by the measured transmission and detection efficiencies of each component of the microscope at ~1534 nm: objective (40%), beam splitter (99%), filter (97%), fiber coupling (87%), and SNSPDs (50 - 85%, depending on optimal vs anti-optimal polarization). The total system efficiency is

therefore: $\eta_{sys} = 0.22 \times 0.40 \times 0.99 \times 0.97 \times 0.87 \times (0.5 - 0.85) = 0.037 - 0.062$, indicating that between ~3.7% - 6.2% of the photons emitted by the sample are ultimately detected.

Experimental Setup

The home-built confocal micro-photoluminescence (μ-PL) setup used in this work is shown schematically in **Supplementary data Figure S12**. Excitation is provided by a narrow-linewidth tunable laser in the telecom band (PurePhotonics PPCL550) or in the visible via an argon-ion laser (Spectra Physics Beamlok 2060) or diode lasers from Omicron (LuxX 457, 488), housed in a dedicated excitation module. The lasers are pulsed using electrical pulses from a Keithley 4225-PMU pulsing card that are fed either to an intensity modulating EOM/AOM or to the amplitude modulation input of the laser. The laser output passes through an appropriate band-pass filter set to further clean up the beam. The beam is then expanded to fill the back aperture of the objective, yielding a diffraction-limited spot on the sample. A Glan-type polarizer (Polarizer 1) cleans up the excitation polarization. The beam is reflected by a 99:1 mirror, with 1% of the laser power directed to the sample module and focused onto the sample by a Zeiss 100x, NA = 0.9, objective lens. The sample is mounted on a closed-loop piezoelectric nanostage (Physik Instrumente) with step resolution of < 2 nm. PL from the sample is collected by the same objective and directed back through the 99:1 transmission beam splitter into the detection module. In resonant telecom PL measurements, the tunable laser is pulsed, and the emission is collected within a time window after the end of the laser pulse. The SNSPD detector bias is shut off during the excitation pulse to prevent latching of the detector. For upconversion PL, a 520, 660, or 980 nm bandpass emission filter is used for the corresponding upconversion measurement. For spectrally resolved measurements, the light is coupled into a single-mode fiber, which sends the signal to a grating spectrometer connected to a pair of superconducting nanowire single-photon detectors (SNSPDs) (Quantum Opus) or a visible PMT. An Andor DV437 camera is used to image the visible PL. For second-order correlation measurements ($g^2(\tau)$), photoluminescence excitation (PLE), or coherence measurements, the emission is directly fiber-coupled to the pair of SNSPDs. These detectors provide high detection efficiency (>85%) and low dark count rates (<40 cps) in the telecom C-band and are interfaced to time-tagging electronics from Swabian Instruments (Time Tagger 20).

All telecom measurements were performed using resonant, pulsed optical excitation of the Er^{3+} transition at 195.4 THz (telecom C-band) and a power of ~90 nW corresponding to a photon flux of $\sim 5 \times 10^{19}$ $cm^{-2}s^{-1}$, followed by detection of PL using SNSPDs. Upconversion measurements are done at an average photon flux of $\sim 2 \times 10^{22}$ $cm^{-2}s^{-1}$. PL detection consisted of a time-delayed fluorescence collection window after the excitation pulse is turned off. For the PLE measurements, the frequency of the tunable laser was broadened by its amplitude modulation response to approximately 50 - 70 MHz under a pulsing repetition rate of ~100 Hz for telecom C-band detection experiments and 20 - 30 MHz under a pulsing repetition rate of ~500 Hz for upconversion-related measurements.[48] The Pure Photonics PPCL550 tunable C-band laser has a noise floor of ~1000 Hz^2/Hz, corresponding to a coherence time of ~80 - 100 μs, determined from frequency-modulation noise power spectral density (PSD) measurements referenced to a calibrated gas-cell absorption standard.[55, 56, 57] This decreases to ~32 μs based on the frequencies relevant to the Ramsey and photon-echo pulsing sequences used in this work. These measurements were performed by Pure Photonics and are reproduced here in **Supplementary Figure S13.**

For Rabi measurements, the system was driven with resonant optical pulses with variable duration t_p. Following each pulse, PL was collected during a fixed 3 ms integration window following a

500 ns delay from the end of the excitation pulse, with a dead time of 5 ms after the integration window. For upconversion measurements, 2-3 sequential telecom pulses tuned +25 MHz from the telecom resonance around 1533.9 nm with 5 μs spacing between pulses are used to excite the Er ions, followed by a detection window of 2 ms with a dead time of 2 ms. The total photon counts were recorded as a function of pulse duration.

Ramsey spectroscopy was employed to probe optical coherence times. Each sequence consisted of two resonant $\pi/2$ pulses (360 ns duration), separated by a variable free evolution time τ_{free}. PL was collected during a fixed 2 ms integration window following a 500 ns delay from the end of the excitation pulse. A 5 ms dead time was included between repetitions to allow full relaxation to the $^4I_{15/2}$ ground state.

A two-pulse photon-echo sequence was also performed on spots containing ensembles of Er ions by applying a $\pi/2$ pulse followed, after a variable free evolution time, by a π pulse. The resulting echo was detected after a second equal free evolution time, and its intensity was recorded as a function of τ_{free} to determine the optical coherence time. The two-pulse photon-echo sequence is well suited for measuring long optical coherence times because it is less sensitive to laser phase fluctuations,[22] as variations in the optical phase of the refocusing π pulse alter the phase of the emitted photon echo but not its intensity, which is measured to determine the coherence time.

Pulsed second-order correlation (g^2) measurements were performed with a resonant π pulse (720 ns duration). PL was collected during either a fixed 3 ms or 10 ms integration window following a 500 ns delay from the end of the excitation pulse. For upconversion measurements, 2-3 sequential resonant telecom pulses (150 ns or 720 ns duration) at ~1533.9 nm with 5 or 200 μs spacing between pulses are used to excite the Er ions, followed by a detection window of 2 ms with a dead time of 2 ms. Temporal gating was implemented using the excitation pulse to define the start and stop of the detection window for both SNSPD channels. Coincidence events between the gated channels were used to construct the second-order correlation function $g^{(2)}(\tau)$.

Correlation functions were fit using the pulsed-$g^2(\tau)$ model[46]

$$g^2(\tau) = y_0 + \sum_i A_i exp\left(\frac{\tau - iT_{rep}}{\tau_{PL}}\right) \qquad [4]$$

where y_0 is a baseline offset, A_i is the amplitude of the i-th peak, iT_{rep} is the center of the i-th peak based on the laser pulse repetition rate, and τ_{PL} is the decay of the peak, which is related to the excited-state lifetime. We determine $g^2(0)$ as the ratio between the integrated area of the zero-time delay peak and the average integrated area of the side peaks. **Supplementary data Table S2** shows a comparison between the extracted excited-state lifetime T_1 and τ_{PL} values between the TRPL measurements and g^2 measurements, respectively.

References

1. K. Alexander, A. Benyamini, D. Black, D. Bonneau, S. Burgos, B. Burridge, H. Cable, G. Campbell, G. Catalano, A. Ceballos, C.-M. Chang, S. S. Choudhury, C. Chung, F. Danesh, T.

Dauer, M. Davis, E. Dudley, P. Er-Xuan, J. Fargas, A. Farsi, et al., A manufacturable platform for photonic quantum computing. Nature 641, 876-883 (2025), doi:10.1038/s41586-025-08820-7.

2. M. Sartison, O. C. Ibarra, I. Caltzidis, D. Reuter, K. D. Jöns, Scalable integration of quantum emitters into photonic integrated circuits. Materials for Quantum Technology 2, 023002 (2022).

3. D. Awschalom, H. Christen, A. Clerk, P. Denes, M. Flatté, D. Freedman, G. Galli, S. Jesse, M. Kasevich, C. Monroe, W. Oliver, C. Palmstrøm, N. Samarth, D. Schlom, I. Siddiqi, T. Taylor, B. Whaley, A. Yacoby, J. Ye, L. Horton, Basic Energy Sciences Roundtable: Opportunities for Basic Research for Next-Generation Quantum Systems. OSTI OAI (U.S. Department of Energy Office of Scientific and Technical Information) (2017), doi:10.2172/1616258.

4. "Strategic Research and Industry Agenda," (available at https://qt.eu/media/pdf/Strategic-Reseach-and-Industry-Agenda-2030.pdf).

5. R. M. Pettit, S. Deckoff-Jones, A. Donis, A. Elias, J. Briscoe, G. Leake, D. Coleman, M. Fanto, A. Sundaresh, S. Gupta, M. K. Singh, S. E. Sullivan, Monolithically Integrated C-Band Quantum Emitters on Foundry Silicon Photonics. Nano Letters 25, 11803-11810 (2025).

6. M. Rančić, M. Hedges, R. Ahlefeldt, M. Sellars, Coherence time of over a second in a telecom-compatible quantum memory storage material. Nature Physics 14, 50-54 (2018).

7. S. Ourari, Ł. Dusanowski, S. P. Horvath, M. T. Uysal, C. M. Phenicie, P. Stevenson, M. Raha, S. Chen, R. J. Cava, N. P. de Leon, J. D. Thompson, Indistinguishable telecom band photons from a single Er ion in the solid state. Nature 620, 977-981 (2023).

8. A. Zalogina, N. Coste, C. Chen, J. Kim, I. Aharonovich, Engineering Quantum Light: Emitters, Photonic Structures, and On-Chip Integration. Laser & Photonics Reviews 20, e02309 (2026), doi:10.1002/lpor.202502309.

9. E. Pelucchi, G. Fagas, I. Aharonovich, D. Englund, E. Figueroa, Q. Gong, H. Hannes, J. Liu, C.-Y. Lu, N. Matsuda, J.-W. Pan, F. Schreck, F. Sciarrino, C. Silberhorn, J. Wang, K. D. Jöns, The potential and global outlook of integrated photonics for quantum technologies. Nature Reviews Physics 4, 194-208 (2022).

10. A. H. Atabaki, S. Moazeni, F. Pavanello, H. Gevorgyan, J. Notaros, L. Alloatti, M. T. Wade, C. Sun, S. A. Kruger, H. Meng, K. Al Qubaisi, I. Wang, B. Zhang, A. Khilo, C. V. Baiocco, M. A. Popović, V. M. Stojanović, R. J. Ram, Integrating photonics with silicon nanoelectronics for the next generation of systems on a chip. Nature 556, 349-354 (2018).

11. K. Azuma, S. E. Economou, D. Elkouss, P. Hilaire, L. Jiang, H.-K. Lo, I. Tzitrin, Quantum repeaters: From quantum networks to the quantum internet. Rev. Mod. Phys. 95, 045006 (2023), doi:10.1103/revmodphys.95.045006.

12. E. Saglamyurek, J. Jin, V. B. Verma, M. D. Shaw, F. Marsili, S. W. Nam, D. Oblak, W. Tittel, Quantum storage of entangled telecom-wavelength photons in an erbium-doped optical fibre. Nature Photonics 9, 83-87 (2015).

13. S. Wehner, D. Elkouss, R. Hanson, Quantum internet: A vision for the road ahead. Science 362, eaam9288 (2018).

14. H. J. Kimble, The quantum internet. Nature 453, 1023-1030 (2008).

15. J. L. O'Brien, A. Furusawa, J. Vučković, Photonic quantum technologies. Nature Photonics 3, 687-695 (2009).

16. Y. Yu, S. Liu, C.-M. Lee, P. Michler, S. Reitzenstein, K. Srinivasan, E. Waks, J. Liu, Telecom-band quantum dot technologies for long-distance quantum networks. Nature Nanotechnology 18, 1389-1400 (2023).

17. M. Anderson, T. Müller, J. Huwer, J. Skiba-Szymanska, A. B. Krysa, R. M. Stevenson, J. Heffernan, D. A. Ritchie, A. J. Shields, Quantum teleportation using highly coherent emission from telecom C-band quantum dots. npj Quantum Information 6, 14 (2020),

18. K. D. Zeuner, M. Paul, T. Lettner, C. Reuterskiöld Hedlund, L. Schweickert, S. Steinhauer, L. Yang, J. Zichi, M. Hammar, K. D. Jöns, V. Zwiller, A stable wavelength-tunable triggered source of single photons and cascaded photon pairs at the telecom C-band. Applied Physics Letters 112, 173102 (2018).

19. Q. Li, J.-F. Wang, F.-F. Yan, J.-Y. Zhou, H.-F. Wang, H. Liu, L.-P. Guo, X. Zhou, A. Gali, Z.-H. Liu, Z.-Q. Wang, K. Sun, G.-P. Guo, J.-S. Tang, H. Li, L.-X. You, J.-S. Xu, C.-F. Li, G.-C. Guo, Room-temperature coherent manipulation of single-spin qubits in silicon carbide with a high readout contrast. National Science Review 9, nwab122 (2022).

20. P. Cilibrizzi, M. J. Arshad, B. Tissot, N. T. Son, I. G. Ivanov, T. Astner, P. Koller, M. Ghezellou, J. Ul-Hassan, D. White, C. Bekker, G. Burkard, M. Trupke, C. Bonato, Ultra-narrow inhomogeneous spectral distribution of telecom-wavelength vanadium centres in isotopically-enriched silicon carbide. Nature Communications 14, 8448 (2023).

21. M. Atatüre, D. Englund, N. Vamivakas, S.-Y. Lee, J. Wrachtrup, Material platforms for spin-based photonic quantum technologies. Nature Reviews Materials 3, 38-51 (2018).

22. L. Yang, S. Wang, M. Shen, J. Xie, H. X. Tang, Controlling single rare earth ion emission in an electro-optical nanocavity. Nature Communications 14, 1718 (2023).

23. Y. Yu, D. Oser, G. D. Prato, E. Urbinati, J. C. Ávila, Y. Zhang, P. Remy, S. Marzban, S. Gröblacher, W. Tittel, Frequency Tunable, Cavity-Enhanced Single Erbium Quantum Emitter in the Telecom Band. Physical Review Letters 131, 170801 (2023).

24. I. R. Berkman, A. Lyasota, G. G. de Boo, J. G. Bartholomew, S. Q. Lim, B. C. Johnson, J. C. McCallum, B.-B. Xu, S. Xie, N. V. Abrosimov, H.-J. Pohl, R. L. Ahlefeldt, M. J. Sellars, C. Yin, S. Rogge, Long optical and electron spin coherence times for erbium ions in silicon. npj Quantum Information 11, 66 (2025).

25. L. R. Weiss, G. T. Smith, R. A. Murphy, B. Golesorkhi, J. A. Méndez Méndez, P. Patel, J. Niklas, O. G. Poluektov, J. R. Long, D. D. Awschalom, A high-resolution molecular spin-photon interface at telecommunication wavelengths. Science 390, 76-81 (2025).

26. S. Gupta, R. M. Pettit, A. Sundaresh, V. Niaouris, S. Deckoff-Jones, D. P. Crowley, L. G. Carpenter, A. M. Dibos, M. K. Singh, S. E. Sullivan, Erbium quantum memory platform with long optical coherence via back-end-of-line deposition on foundry-fabricated photonics. Physical Review Applied 24, 014056 (2025).

27. S. Wang, L. Yang, M. Shen, W. Fu, Y. Xu, R. L. Cone, C. W. Thiel, H. X. Tang, Er:LiNbO3 with High Optical Coherence Enabling Optical Thickness Control. Physical Review Applied 18, 014069 (2022).

28. S. Castelletto, C. T.-K. Lew, W.-X. Lin, J.-S. Xu, Quantum systems in silicon carbide for sensing applications. Reports on Progress in Physics 87, 014501 (2024).

29. C. P. Anderson, A. Bourassa, K. C. Miao, G. Wolfowicz, P. J. Mintun, A. L. Crook, H. Abe, J. Ul Hassan, N. T. Son, T. Ohshima, D. D. Awschalom, Electrical and optical control of single spins integrated in scalable semiconductor devices. Science 366, 1225-1230 (2019).

30. D. D. Awschalom, R. Hanson, J. Wrachtrup, B. B. Zhou, Quantum technologies with optically interfaced solid-state spins. Nature Photonics 12, 516-527 (2018).

31. A. K. Rebane, C. W. Thiel, R. K. Mohan, R. L. Cone, Slow decoherence and the radiative decay limit in rare-earth-doped crystals for coherent optical storage. Bull. Russ. Acad. Sci. Phys. 74, 891-900 (2010), doi:10.3103/S1062873810070014.

32. M. Rančić, M. Le Dantec, S. Lin, S. Bertaina, T. Chanelière, D. Serrano, P. Goldner, R. B. Liu, E. Flurin, D. Estève, D. Vion, P. Bertet, Electron-spin spectral diffusion in an erbium doped crystal at millikelvin temperatures. Physical Review B 106, 144412 (2022).

33. N. Tabassum, V. Nikas, A. E. Kaloyeros, V. Kaushik, E. Crawford, M. Huang, S. Gallis, Engineered telecom emission and controlled positioning of Er^{3+} enabled by SiC nanophotonic structures. Nanophotonics 9, 1425-1437 (2020).

34. D. Lukin, C. Dory, M. A. Guidry, K. Y. Yang, S. D. Mishra, R. Trivedi, M. Radulaski, S. Sun, D. Vercruysse, G. H. Ahn, J. Vučković, 4H-silicon-carbide-on-insulator for integrated quantum and nonlinear photonics. Nature Photonics 14, 330-334 (2020).

35. A. Lohrmann, B. C. Johnson, J. C. McCallum, S. Castelletto, A review on single photon sources in silicon carbide. Reports on Progress in Physics 80, 034502 (2017).

36. S. Gallis, V. Nikas, H. Suhag, M. Huang, A. E. Kaloyeros, White light emission from amorphous silicon oxycarbide (a-SiCxOy) thin films: Role of composition and postdeposition annealing. Applied Physics Letters 97, 081905 (2010).

37. S. Dutta, A. Kaloyeros, A. Nanaware, S. Gallis, Scalable Chemical Vapor Deposition of Silicon Carbide Thin Films for Photonic Integrated Circuit Applications. Applied Sciences 15, 8603 (2025).

38. A. Yi, C. Wang, L. Zhou, M. Zhou, S. Zhang, T. You, J. Zhang, X. Ou, Silicon carbide for integrated photonics. Applied Physics Reviews 9, 031302 (2022).

39. J. Wong, M. Onizhuk, J. Nagura, A. S. Thind, J. K. Bindra, C. Wicker, G. D. Grant, Y. Zhang, J. Niklas, O. G. Poluektov, R. F. Klie, J. Zhang, G. Galli, F. J. Heremans, D. D. Awschalom, A. P. Alivisatos, Coherent Erbium Spin Defects in Colloidal Nanocrystal Hosts. ACS Nano 18, 19110-19123 (2024).

40. A. Singh, K. Dev, H. Siljak, H. D. Joshi, M. Magarini, Quantum Internet—Applications, Functionalities, Enabling Technologies, Challenges, and Research Directions. IEEE Communications Surveys & Tutorials 23, 2218-2247 (2021).

41. N. Tabassum, M. Kotha, V. Kaushik, B. Ford, S. Dey, E. Crawford, V. Nikas, S. Gallis, On-Demand CMOS-Compatible Fabrication of Ultrathin Self-Aligned SiC Nanowire Arrays. Nanomaterials 8, 906 (2018).

42. M. G. Wood, L. Chen, J. R. Burr, R. M. Reano, Optimization of electron beam patterned hydrogen silsesquioxane mask edge roughness for low-loss silicon waveguides. Journal of Nanophotonics 8, 083098 (2014).

43. K. Groot-Berning, T. Kornher, G. Jacob, F. Stopp, S. T. Dawkins, R. Kolesov, J. Wrachtrup, K. Singer, F. Schmidt-Kaler, Deterministic Single-Ion Implantation of Rare-Earth Ions for Nanometer-Resolution Color-Center Generation. Physical Review Letters 123, 106802 (2019).

44. J. Lee, V. Leong, D. Kalashnikov, J. Dai, A. Gandhi, L. A. Krivitsky, Integrated single photon emitters. AVS Quantum Science 2, 031701 (2020).

45. I. Aharonovich, D. Englund, M. Toth, Solid-state single-photon emitters. Nature Photonics 10, 631-641 (2016).

46. C. Zhu, M. Marczak, L. Feld, S. C. Boehme, C. Bernasconi, A. Moskalenko, I. Cherniukh, D. Dirin, M. I. Bodnarchuk, M. V. Kovalenko, G. Rainò, Room-Temperature, Highly Pure Single-Photon Sources from All-Inorganic Lead Halide Perovskite Quantum Dots. Nano Letters 22, 3751-3760 (2022).

47. A. M. Dibos, M. T. Solomon, S. E. Sullivan, M. K. Singh, K. E. Sautter, C. P. Horn, G. D. Grant, Y. Lin, J. Wen, F. J. Heremans, S. Guha, D. D. Awschalom, Purcell Enhancement of Erbium Ions in TiO2 on Silicon Nanocavities. Nano Letters 22, 6530-6536 (2022).

48. "Amplitude Modulation Application note: AM input," (available at https://purephotonics.com/wp-content/uploads/Application-note-AM-input.pdf).

49. A. Kaloyeros, S. Dutta, S. Gallis, Engineering and polarization properties of erbium-implanted lithium niobate films for integrated quantum applications. APL Materials 12, 071101 (2024).

50. S. Gallis, M. Huang, A. E. Kaloyeros, Efficient energy transfer from silicon oxycarbide matrix to Er ions via indirect excitation mechanisms. Applied Physics Letters 90, 161914 (2007).

51. B. Ford, N. Tabassum, V. Nikas, S. Gallis, Strong Photoluminescence Enhancement of Silicon Oxycarbide through Defect Engineering. Materials 10, 446 (2017).

52. S. Gallis, V. Nikas, A. E. Kaloyeros, Silicon Oxycarbide Thin Films and Nanostructures: Synthesis, Properties and Applications, in Modern Technologies for Creating the Thin-film Systems and Coatings (InTech, 2017).

53. I. D. Abella, N. A. Kurnit, S. R. Hartmann, Photon Echoes. Phys. Rev. 141, 391-406 (1966).

54. R. M. Macfarlane, R. Wannemacher, D. Boye, Y. P. Wang, R. S. Meltzer, Nonexponential photon echo decay of Er^{3+} in fluorides. Journal of Luminescence 48-49, 313-317 (1991).

55. "Application note: Amplitude and Frequency noise," (available at https://purephotonics.com/wp-content/uploads/Application-Note-PPCL700-noise-measurements-revB.pdf).

56. "Laser linewidth measurements - Application Note," (available at https://purephotonics.com/wp-content/uploads/application-note-Linewidth-Measurement.pdf).

57. G. Di Domenico, S. Schilt, P. Thomann, Simple approach to the relation between laser frequency noise and laser line shape. Applied Optics 49, 4801-4807 (2010).

Supplementary Files

This is a list of supplementary files associated with this preprint. Click to download.

- NatureNTSupplementaryInformationFClean.pdf